

APPLIED PHYSICS

Continuous angle-tunable birefringence with freeform metasurfaces for arbitrary polarization conversion

Zhujun Shi¹, Alexander Y. Zhu², Zhaoyi Li², Yao-Wei Huang^{2,3}, Wei Ting Chen², Cheng-Wei Qiu³, Federico Capasso^{2,*}

Birefringence occurs when light with different polarizations sees different refractive indices during propagation. It plays an important role in optics and has enabled essential polarization elements such as wave plates. In bulk crystals, it is typically constrained to linear birefringence. In metamaterials with freeform meta-atoms, however, one can engineer the optical anisotropy such that light sees different indices for arbitrary—linear, circular, or elliptical—orthogonal eigen-polarization states. Using topology-optimized metasurfaces, we demonstrate this arbitrary birefringence. It has the unique feature that it can be continuously tuned from linear to elliptical birefringence, by changing the angle of incidence. In this way, a single metasurface can operate as many wave plates in parallel, implementing different polarization transformations. Angle-tunable arbitrary birefringence expands the scope of polarization optics, enables compact and versatile polarization operations that would otherwise require cascading multiple elements, and may find applications in polarization imaging, quantum optics, and other areas.

INTRODUCTION

Birefringence, defined by the polarization dependence of refractive indices, plays a role of paramount importance in manipulating the polarization states of light. Traditionally, birefringence is considered as an intrinsic property of certain materials (Fig. 1A), such as calcite (1). Despite their widespread use, these devices are bulky and offer limited control over the angular or spectral response. Shape birefringence, in contrast, results from the anisotropic shape of constituting structural elements rather than material anisotropy. It has been investigated in optical fibers (2), waveguides (3), and, more recently, metasurfaces (4–8)—planar optical components consisting of nanostructures patterned at a subwavelength scale. Metasurface shape birefringence offers a great variety of design degrees of freedom for tailoring device's polarization response and, therefore, has emerged as a versatile platform for polarization optics (9–12).

Previous metasurface shape birefringence devices suffer from two limitations: restricted choice of eigen-polarization states and lack of angular control. Previous studies mainly consider simple symmetric shapes, which fundamentally limits the choice of eigen-polarization states and, thus, the devices' polarization functions (7, 8, 11). Most existing devices are restricted to be either linearly or circularly birefringent owing to symmetry constraints. Despite their prevalence, they constitute only a small subset of all possibilities. In general, realizing an arbitrary lossless polarization transformation requires having elliptical birefringence, i.e., birefringent components whose eigen-polarization states are elliptically polarized (13, 14). Representing the most general case, it unlocks the full potential of polarization control: A single elliptically birefringent component is capable of implementing arbitrary unitary polarization transformation, which otherwise would require cascading multiple linearly or circularly birefringent components (13–15). This is especially relevant in advanced polarization optics and quantum optics where compact

implementation of versatile polarization control is of vital importance. However, so far, the capability to tailor arbitrary elliptical birefringence has not been explored.

Second, the angular response of shape birefringence, which is an essential degree of freedom to manipulate light, has not been well investigated. Engineered angle-dependent optical response not only enables easy integration of multiple functions in a single device controlled by the angle of incidence, i.e., angle tunable multifunctionality, but also allows for unconventional light manipulation in momentum (k) space (16) (in contrast to the usual real space operation). However, since previous studies focus primarily on normal incidence operation, the angular dependence is usually ignored or treated as an unwanted artifact. Recently, researchers have started to investigate the behavior of metasurfaces at oblique angles of incidence. However, these studies either use plasmonic structures that are inherently lossy (17) or consider phase-only holograms that provide no polarization transformation capability (18). The interplay between angle and polarization degrees of freedom in metasurfaces has remained largely unexplored.

To address these limitations, we use the adjoint-based topological optimization, a photonic inverse design technique, to engineer the birefringent response of metasurface elements (19–25). Topological optimization allows the shape of nanostructures to be varied continuously in the design domain to minimize a given cost function subject to functional and geometrical constraints (19–25). Compared with the forward design strategy that relies on parameter sweeps of simple regular shapes, topological optimization provides a considerably larger design space, allowing searching for nonintuitive structures. This opens possibilities to engineering unconventional birefringent response of metasurfaces. It is worth noting that, in principle, elliptical birefringence might exist in any structure with broken symmetries (section S1). However, without optimization, these effects are usually weak and uncontrollable (section S3.3). Here, with topological optimization, we are able to intentionally tailor the desired elliptical birefringence as a functional feature.

Using topological optimization, we demonstrate arbitrary shape birefringence (Fig. 1C) that addresses the abovementioned limitations.

Copyright © 2020
The Authors, some
rights reserved;
exclusive licensee
American Association
for the Advancement
of Science. No claim to
original U.S. Government
Works. Distributed
under a Creative
Commons Attribution
NonCommercial
License 4.0 (CC BY-NC).

¹Harvard Department of Physics, Harvard University, Cambridge, MA 02138, USA.

²Harvard John A. Paulson School of Engineering and Applied Sciences, Harvard University, Cambridge, MA 02138, USA. ³Department of Electrical and Computer Engineering, National University of Singapore, Singapore 117583, Singapore.

*Corresponding author. Email: capasso@seas.harvard.edu

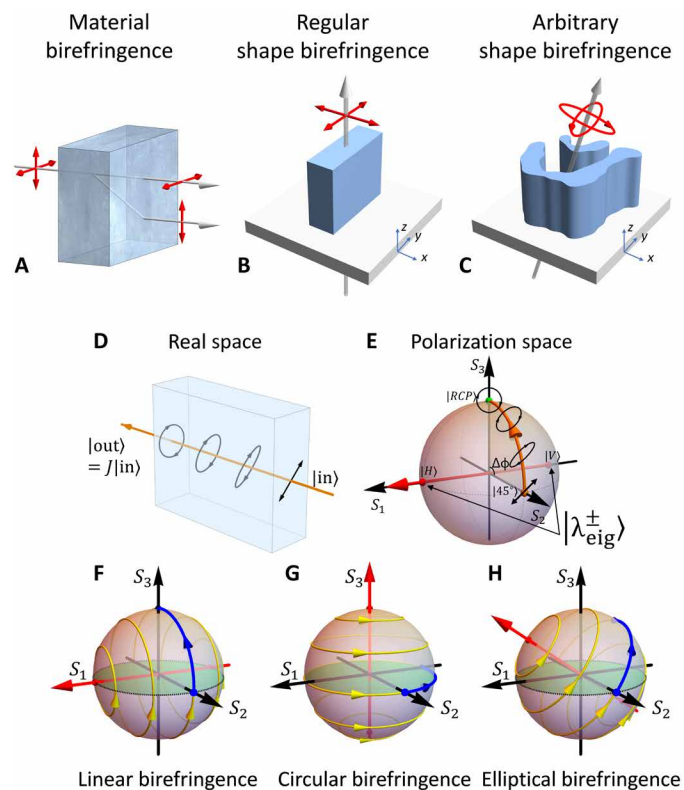


Fig. 1. Concept of arbitrary elliptical birefringence. (A) Material birefringence results from intrinsic material anisotropy. (B) Regular shape birefringence considers simple symmetric structures at normal incidence. The red arrows represent the linearly polarized eigenstates. (C) Arbitrary shape birefringence uses freeform structures to unlock novel polarization functionalities. In this work, we demonstrate a device that can be continuously tuned from linear birefringence to elliptical birefringence by varying the angle of incidence. The red arrows represent the elliptical eigen-polarization states at oblique incidence. (D) The evolution of polarization state of a light beam propagating through a quarter-wave plate in the real space. (E) The same polarization evolution can be represented as a rotation (orange curve) in the polarization space (i.e., Poincaré sphere). (F to H) Polarization space representation of (F) linear, (G) circular, and (H) elliptical birefringence. In general, birefringence induces a rotation of polarization states on the Poincaré sphere (along the yellow lines), with the rotation axis (red axis) and rotation angle determined by the device's eigen-polarization states (red dots) and retardance, respectively. The blue arrows show the trajectories for a quarter-wave retardance assuming a 45° linearly polarized incident light.

It features a freeform shape, tailorable eigen-polarization states and designed angle tunability. It can be continuously tuned from linear birefringence to elliptical birefringence for various angles of incidence. At each fixed oblique angle of incidence, the tailored elliptical birefringence allows for versatile polarization transformation beyond what is achievable with previous single-layer metasurfaces. For a range of angles of incidence, the designed angle tunability enables multifunctional polarization manipulation in momentum space. Our approach has a wide range of potential applications across industry and scientific research, such as momentum-space vector beam generation and polarization aberration correction in advanced optical systems.

Design principle

In the absence of polarization-dependent transmission efficiency difference, any birefringence breaks the polarization degeneracy of

light to produce two orthogonally polarized modes that travel with different phase velocity. These two special polarization states are the eigen-polarization states of the device, i.e., the characteristic polarization states that remain unchanged upon propagation. Any other incident state will, in general, undergo polarization conversion according to its projection onto the eigen-polarization state basis. Up to an overall phase, the eigen-polarization states, together with the retardance, defined by the phase difference between the two eigen-polarization states accumulated during propagation, fully determine the polarization function of any birefringent device.

Explicitly, the polarization effect of a birefringent component is described by its Jones matrix J , which can be expressed in terms of an overall phase $\bar{\phi}$, the retardance $\Delta\phi$, and the eigen-polarization states $|\lambda_{\text{eig}}^{\pm}\rangle$ in bra-ket notation (14)

$$J = e^{i\bar{\phi}} \left[e^{i\frac{\Delta\phi}{2}} |\lambda_{\text{eig}}^{+}\rangle\langle\lambda_{\text{eig}}^{+}| + e^{-i\frac{\Delta\phi}{2}} |\lambda_{\text{eig}}^{-}\rangle\langle\lambda_{\text{eig}}^{-}| \right]$$

Among the three quantities, the overall phase $\bar{\phi}$ and retardance $\Delta\phi$ have been widely investigated and used in metasurface design for versatile wavefront shaping (5, 7, 8). They can be easily adjusted, for example, by changing the length and width of simple rectangular nanopillars. In contrast, despite their fundamental role, the ability to engineer the eigen-polarization states $|\lambda_{\text{eig}}^{\pm}\rangle$ remains elusive, primarily due to the inherent symmetry constraints in previous designs.

At normal incidence, the symmetry of the geometric shape of the structure elements dictates the eigen-polarization states of the device, regardless of the specific realization (section S1) (26, 27). For example, patterns that have mirror symmetry with respect to the xz or yz plane (M_{xz} or M_{yz}) are bound to be linearly birefringent (Fig. 1B). Here, xy is the metasurface plane and z is the surface normal direction. This constitutes a majority of previous metasurface devices. The advantage of such choice is its design simplicity; however, it sacrifices the versatility of achievable polarization operation.

In general, realizing an arbitrary lossless polarization transformation necessitates having elliptical birefringence, i.e., birefringent components whose eigen-polarization states are elliptically polarized (13, 14). For example, consider a simple task where one wants to convert horizontal polarization to 45° linear polarization ($|H\rangle \rightarrow |45^{\circ}\rangle$) and left circular polarization to horizontal polarization ($|LCP\rangle \rightarrow |H\rangle$). Here, we consider two different input states because the polarization function is characterized by a 2×2 matrix (the Jones matrix), and at least two input-output mappings are required to characterize the device. This task is impossible with a single linearly birefringent device. However, with a properly designed elliptical birefringent wave plate, both operations can be fulfilled with a single component (fig. S3). Therefore, it is critical to have elliptically birefringent devices to facilitate compact implementation of arbitrary polarization control.

For clarity, it is worthwhile to mention the difference between eigen-polarization states and operating polarization states, i.e., the designed incident polarization states. A recently proposed class of metasurfaces (8) use elliptical polarization as the operating state, but the eigenstates of each nanopillar are still linear. As a consequence, the output is converted to the conjugate of input polarization state (8). Such inevitable polarization conversion, which is often unwanted, is another manifestation of the limitations of previous linear shape birefringence devices.

To realize arbitrary eigen-polarization states that overcome these limitations, we design a freeform metasurface that has highly nonintuitive shapes and has no in-plane symmetry. This, in principle, allows for arbitrary shape birefringence beyond what is achievable with regular shapes. We further couple the birefringent response to the angular degree of freedom. The introduction of angle dependence is important as it removes any residual symmetry constraints. Since the designed structure is single layer and vertical, it is approximately mirror symmetric with respect to the xy plane (M_{xy}). This symmetry is exact in the absence of substrate and still holds in an approximate manner in actual devices with substrates (26, 28). Without additional dichroism, systems with M_{xy} symmetry must be linearly birefringent (section S1). However, for oblique angles of incidence, this symmetry is broken for the overall optical system, which includes not only the metasurface structures but also the incident light rays (section S1). As a result, the system can acquire arbitrary eigen-polarization states for oblique incidence (section S2).

To provide an intuitive picture of this concept of arbitrary shape birefringence, we use the polarization space (Poincaré sphere) representation of birefringent components. Poincaré sphere is a graphical tool for visualizing polarization states. Each point on the surface of the sphere represents a fully polarized state, with the Cartesian coordinates given by the normalized Stokes parameters $(\frac{S_1}{S_0}, \frac{S_2}{S_0}, \frac{S_3}{S_0})$ (14). The north and south poles represent right and left circular polarization and points on the equator correspond to linear polarization states. Using this picture, the polarization effects of birefringence can be elegantly described as a rotation on the Poincaré sphere, with the rotation axis and rotation angle determined by the eigen-polarization states $|\lambda_{\text{eig}}^{\pm}\rangle$ and retardance $\Delta\phi$, respectively (Fig. 1E). As an illustrative example, the polarization effects of a conventional quarter-wave plate are shown both in real space (Fig. 1D) and on the Poincaré sphere (Fig. 1E). In real space, 45° linearly polarized incident light is gradually converted to right circular polarization at the output, $|45^\circ\rangle \rightarrow |RCP\rangle$ (Fig. 1D). If we trace the polarization evolution on the Poincaré sphere, it follows a circular trajectory (Fig. 1E) that corresponds to a rotation around the S_1 axis by $\pi/2$. Note that the rotation axis connects the two eigen-polarization states, $|H\rangle$ and $|V\rangle$ in this case. The $\pi/2$ rotation angle results from the quarter-wave retardance ($\lambda/4$).

This geometrical representation provides a unified picture for visualizing the polarization effects of different types of birefringence. Linear birefringence is represented by rotations on the Poincaré sphere around an axis that is limited to be within the equatorial plane (Fig. 1F). Circular birefringence features a rotation axis that coincides with the S_3 axis (Fig. 1G). Despite their prevalence, linear and circular birefringence constitutes only a small subset of all possible birefringence. Elliptical birefringence, in contrast, can take arbitrary rotation axes (Fig. 1H). It represents the most general type of birefringence and allows versatile polarization transformation beyond what is achievable with single linearly or circularly birefringent components.

A schematic of the topology-optimized structure element is shown in Fig. 2A. It consists of 1.5- μm -thick silicon nanostructures with optimized cross-sectional shape, on top of a glass substrate. The center-to-center distance between adjacent structures (U) is 600 nm. The design operating wavelength is 1550 nm. Here, the unit cell size U is chosen to be small enough to eliminate any higher-

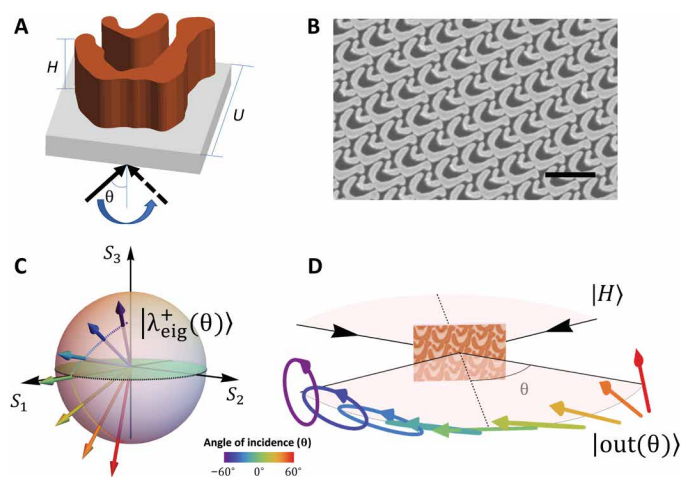


Fig. 2. Topology-optimized structure element. (A) Schematic of the optimized structure. It consists of freeform amorphous silicon (a-Si) nanostructures patterned on top of a glass substrate. The a-Si thickness is $H = 1500$ nm. The center-to-center distance between neighboring elements is $U = 600$ nm. (B) SEM image of a fabricated sample. Scale bar, 1 μm . (C) The arrows represent the angle-dependent eigen-polarization states ($|\lambda_{\text{eig}}^+(\theta)\rangle$) of the device. Different colors correspond to different angles of incidence (θ). As one varies the angle, the device can be continuously tuned between linear and elliptical birefringence. (D) Angle-dependent polarization generation. For a fixed incident polarization ($|in\rangle = |H\rangle$), the output polarization state ($|out(\theta)\rangle = J(\theta)|H\rangle$) changes continuously from right circular polarization through horizontal linear polarization to 45° linear polarization for varying angle of incidence.

order diffraction across the entire angular range. A small U is also critical for obtaining a relatively smooth and continuous angular response, as the number of guided mode resonances grows rapidly with increasing unit cell size (29). On the other hand, however, given the minimal feature size, a larger unit cell size offers a larger design space and is easier to fabricate. Our choice of unit cell size reflects a balance of the abovementioned considerations. More details about the implementation of topological optimization can be found in the Supplementary Materials (section S2). Figure 2B shows a top-view SEM image of a fabricated sample.

The functionality of our device can be illustrated on the Poincaré sphere (Fig. 2C). As the angle of incidence varies, the eigen-polarization state $|\lambda_{\text{eig}}^+\rangle$ follows a trajectory on the Poincaré sphere that protrudes from the equator, highlighting the transition from linear to elliptical birefringence. It is also convenient to consider the polarization effects from an input-output point of view, $|out\rangle = J|in\rangle$. For a fixed input polarization state, horizontal linear polarization $|H\rangle$, the output polarization state is designed to change continuously from right circular polarization through horizontal linear polarization to 45° linear polarization for various angles of incidence (Fig. 2D). This enables new methods of polarization control in the momentum space, as the device induces different polarization transformations for different momentum (angle) components of a light beam.

RESULTS

To fully characterize the device's polarization response, Mueller matrix polarimetry (30) was performed at various angles of incidence (section S4). Figure 3 shows the measured and simulated polarization states at $\theta = -60^\circ, 0^\circ$, and 60° . The device's functionality is illustrated

using the polarization space (Poincaré sphere) representation for each angle (Fig. 3A). Figure 3B shows the measured (black) and simulated (brown) eigen-polarization state, $|\lambda_{\text{eig}}^{\pm}\rangle \sim J|\lambda_{\text{eig}}^{\pm}\rangle$. We use the “ \sim ” symbol instead of the equals sign because, in general, the eigenstate will acquire a phase shift. One can see that at normal incidence, $|\lambda_{\text{eig}}^{\pm}\rangle$ are linearly polarized, whereas at oblique incidence, $|\lambda_{\text{eig}}^{\pm}\rangle$ become elliptically polarized. Both the ellipticity and the orientation of the eigen-polarization ellipses differ substantially from that at normal incidence, proving the effectiveness of our design strategy. As expected from the unitarity of the Jones matrices (section S1), $|\lambda_{\text{eig}}^{\pm}\rangle$ and $|\lambda_{\text{eig}}^{\mp}\rangle$ are approximately orthogonal to each other at each angle of incidence. Note that the eigen-polarization states at $\pm 60^\circ$ have opposite handedness (section S2.2). Figure 3C shows the output polarization states for a fixed incident state (horizontal linear polarization $|H\rangle$). By design, the incident light is converted into right circular polarization $|RCP\rangle$, horizontal linear polarization $|H\rangle$, and 45° linear polarization $|45^\circ\rangle$ at $\theta = -60^\circ, 0^\circ$, and 60° , respectively (brown polarization ellipses). The measured output polarization states, $|\text{out}\rangle = J|H\rangle$, are shown in black in Fig. 3C. The measured degree of circular polarization (DOCP) (14) is 0.94 at -60° . The measured degree of linear polarization (DOLP) (14) is 0.99 and 0.96 at $\theta = 0^\circ, 60^\circ$ respectively. The discrepancy between the simulation and measurement could be explained by fabrication errors such as structure dilation and inaccurate thickness (section S3). Despite the difference, the phenomenon of interest—elliptical birefringence and unconventional angular dependence—remains robust.

The measured eigen-polarization states $|\lambda_{\text{eig}}^{\pm}\rangle \sim J|\lambda_{\text{eig}}^{\pm}\rangle$ for a continuous angular range are shown in Fig. 4 (A and B). Each point on the Poincaré sphere corresponds to a polarization state measured

at a specific angle (indicated by the color). To interpret the result, remember that the latitude and longitude on the Poincaré sphere are related to the ellipticity and orientation of polarization ellipses, respectively (fig. S7). One can see that both the ellipticity and the orientation of the eigen-polarization states vary significantly as a function of angle. Such strong and exotic angular dependence of eigen-polarization states has not been observed in previous birefringent components. Note that at each angle, the two eigen-polarization states ($|\lambda_{\text{eig}}^{\pm}\rangle$ and $|\lambda_{\text{eig}}^{\mp}\rangle$) are located approximately at opposite points [$(S_1, S_2, S_3) \leftrightarrow (-S_1, -S_2, -S_3)$] on the Poincaré sphere, indicating their orthogonality. Figure 4C shows the output polarization $|\text{out}\rangle = J|H\rangle$ as a function of the angle of incidence. It follows an unconventional trajectory on the Poincaré sphere connecting the north pole $|RCP\rangle$ and the S_2 axis $|45^\circ\rangle$. The insets highlight the schematic and measured polarization ellipses at 0° and $\pm 60^\circ$.

From the measured Mueller matrices, we extracted the transmission efficiency for each eigen-polarization (Fig. 4D), as well as the retardance (Fig. 4E). The transmission efficiency is around 80% at normal incidence and gradually drops to around 65% for larger angles. The difference between the efficiency for the two eigen-polarizations is small, proving that the polarization effect is primarily birefringence rather than dichroism. Two pairs of accidental guided mode resonances were observed at $\pm 6^\circ$ and $\pm 26^\circ$. They are responsible for the data points scattered away from the regression line in Fig. 4 (A to C). The guided mode resonances can be eliminated in future designs by reducing the unit cell size or adding constraints in the optimization. Compared to the eigen-polarization states, the overall change in retardance (Fig. 4E) is less marked, maintaining a value around $\lambda/4$ ($\pi/2$). This is in sharp contrast with previous studies of metasurfaces' angular response (17, 18). There, the eigen-polarization states

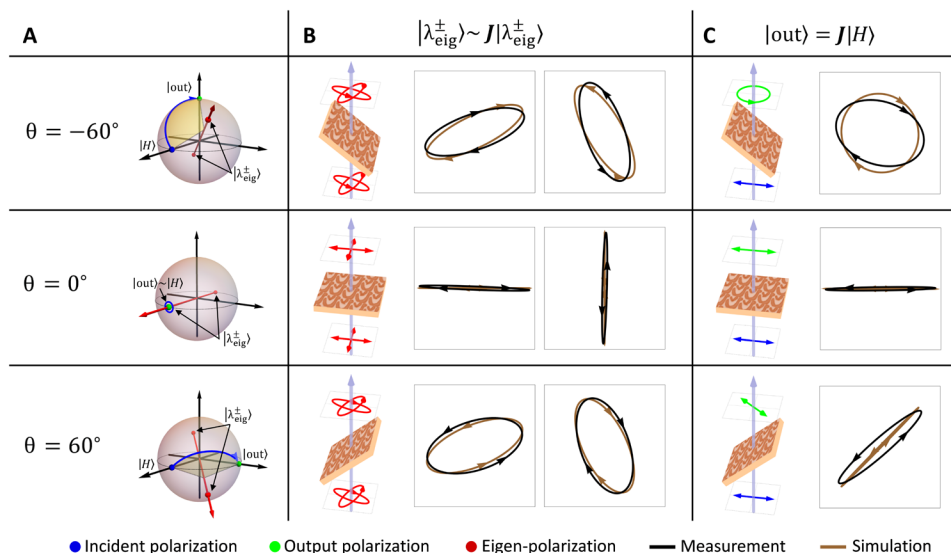


Fig. 3. Measurement results at the angles of incidence $\theta = -60^\circ, 0^\circ$, and 60° . (A) Polarization space representation of the device functionality. At each angle, the device induces a rotation (blue arrows) on the Poincaré sphere, which converts the input polarization ($|H\rangle$, blue dots) to the output polarization states ($|\text{out}\rangle$, green dots). The rotation axis (red arrows) is determined by the device's eigen-polarization states ($|\lambda_{\text{eig}}^{\pm}\rangle$, red dots). (B) Measured (black) and simulated (brown) eigen-polarization states ($|\lambda_{\text{eig}}^{\pm}\rangle$). One can see that at $\pm 60^\circ$, the device is elliptically birefringent [corresponding to the out-of-equatorial-plane rotation axis in (A)], whereas at normal incidence, the device is linearly birefringent. At each angle, the two eigen-polarization states, $|\lambda_{\text{eig}}^{\pm}\rangle$ and $|\lambda_{\text{eig}}^{\mp}\rangle$, are approximately orthogonal to each other. Note that the eigen-polarization states at $\pm 60^\circ$ have opposite handedness. (C) Measured (black) and simulated (brown) output polarization states ($|\text{out}\rangle$) for a fixed incident polarization $|H\rangle$. By design, the output polarization becomes right circular polarization, horizontal linear polarization, and 45° linear polarization at $\theta = -60^\circ, 0^\circ$, and 60° respectively. The measured DOCP (14) is 0.94 at -60° . The measured DOLP (14) is 0.99 and 0.96 at $\theta = 0^\circ, 60^\circ$ respectively.

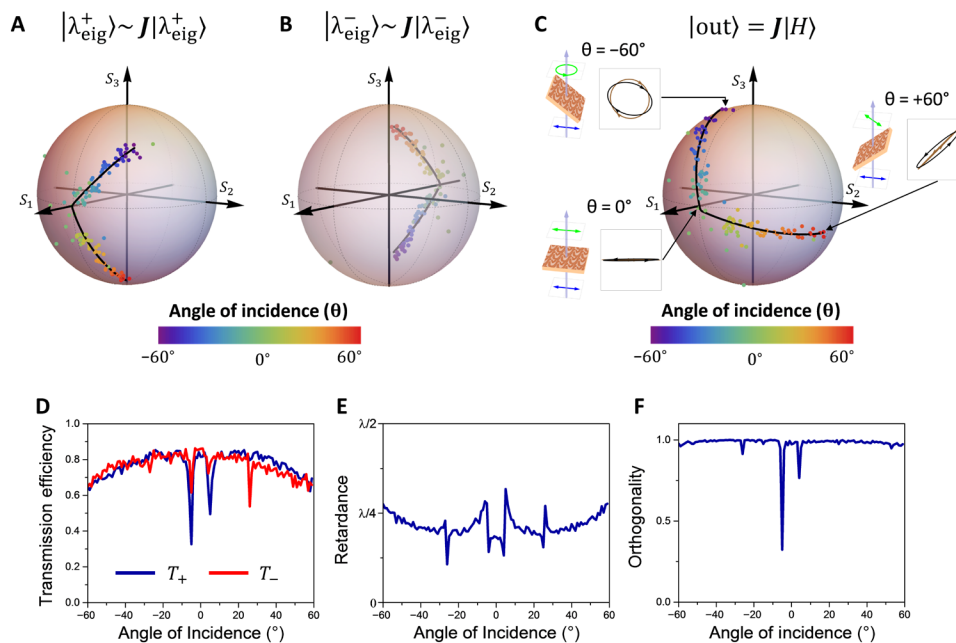


Fig. 4. Measurement results for a continuous angular range. (A and B) Measured eigen-polarization states $|\lambda_{\text{eig}}^\pm\rangle$ at various angles of incidence. The color represents the angle of incidence (θ). Both the ellipticity and the orientation, which is related to the latitude and longitude of the Poincaré sphere, respectively (fig. S7), of the eigen-polarization states vary significantly as a function of the angle of incidence. The solid black line is a fitted curve of the trajectory. (C) Measured output polarization states ($|\text{out}\rangle$) for a fixed incident polarization state $|H\rangle$. As θ angle changes from -60° to 60° , the output polarization state follows a nonconventional trajectory on the Poincaré sphere, which goes continuously from nearly right circular polarization (S_3) through horizontal linear polarization (S_1) to nearly 45° linear polarization (S_2). The schematic, as well as the measured (black) and simulated (brown) polarization ellipses at 0° and $\pm 60^\circ$, are highlighted in the insets. (D) Measured transmission efficiency for the two eigen-polarization states $|\lambda_{\text{eig}}^+\rangle$ (blue line) and $|\lambda_{\text{eig}}^-\rangle$ (red line). The transmission dips result from excitation of guided mode resonances. (E) Measured retardance. (F) Measured orthogonality of the two eigen-polarization states. It is defined as $1 - |\langle \lambda_{\text{eig}}^+ | \lambda_{\text{eig}}^- \rangle|^2$. Away from the resonances, the two eigenstates are almost orthogonal.

remain the same regardless of the angle, and the angular dispersion results predominately from the change of retardance (i.e., phase) (17, 18). We also computed the orthogonality, $1 - |\langle \lambda_{\text{eig}}^+ | \lambda_{\text{eig}}^- \rangle|^2$, of the two eigen-polarization states (Fig. 4F). One can see that except from the resonances, the orthogonality remains high and close to 1. To investigate the underlying physical mechanism, we analyzed the Bloch modes supported in the metasurface layer (section S5) (31). Four propagating Bloch modes are identified inside the nanostructures (fig. S9). Mode analysis suggests that the observed unconventional polarization response is dominated by the two lowest-order Bloch modes, whereas the guided mode resonances are related to the excitation of higher-order Bloch modes.

DISCUSSION

Here, we realized tailorable elliptical birefringence using artificial metasurfaces. In nature, there are also a few examples of elliptical birefringence. For instance, alpha-quartz has a special crystal structure such that it becomes elliptically birefringent along certain crystal orientations (32). Elliptical birefringence has also been observed in spun optical fibers (33). In spun optical fibers, the circular birefringence induced by a fiber twist adds to the intrinsic linear birefringence of the core and results in elliptically polarized eigenmodes. However, in these cases, not only are the effects typically small but also they are very challenging to design and control.

To achieve elliptical birefringence, it is critical to break the M_{xy} symmetry. Here, it is done by using oblique angles of incidence, which has the advantage of versatile angular tunability and multi-function. Note, however, that the M_{xy} symmetry can also be broken by using multilayer metasurfaces, or single-layer metasurfaces with slanted nanostructures. In these cases, one may realize elliptical birefringence at normal incidence.

Using a photonic inverse design technique, we demonstrated a freeform metasurface with angle-tunable elliptical birefringence. It has a wide range of scientific and industrial applications. For example, it enables new methods of vector beam generation, where different momentum (angle) components of a light beam can be converted to different polarization states. This corresponds to generating vector beams in momentum space and may find applications in optical communications (14). If combined with a polarization camera (11), our device can also be used for wavefront sensing, where the local momentum (k direction (angle) of the wavefront can be determined by observing the local polarization states. Another potential application is polarization aberration correction. In complex optical systems, significant aberrations may occur due to accumulated polarization errors. Correcting these errors usually require applying distinct polarization transformations to different field (angle) components (13). In this case, the ability to tailor the polarization response over a range of angles, and in a compact package, becomes essential to reducing the polarization aberration and improving the imaging quality. Our work significantly expands the scope of metasurface polarization

optics and allows for a wide variety of new polarization-related devices.

MATERIALS AND METHODS

Optimization procedure

We used the open source rigorous coupled-wave analysis solver RETICOLO for electromagnetic simulation (34). The optimization is implemented using the MATLAB built-in optimization toolbox. A random continuous initial refractive index pattern is generated without preset symmetry constraints. For each iteration, forward and adjoint simulations are performed for $\theta = 0^\circ, \pm 60^\circ$ to compute the gradient and to update the refractive index profile. Robustness is built in by simultaneously considering the diluted, intermediate, and eroded pattern. Gaussian filters are used to remove small sharp features and to achieve a connected pattern. A hyperbolic tangent function is applied to gradually push the continuous refractive index profile to discrete structures which contain only air and silicon. The optimization is performed iteratively and typically converges within 300 iterations.

Measurement setup

To fully characterize the device's polarization response, dual-rotating retarder Mueller matrix polarimetry (30) was performed at various angles of incidence (fig. S8). The setup has five sections: the laser source, the polarization state generator (PSG), the metasurface sample (mounted on a rotation stage), the polarization state analyzer (PSA), and the detector. An iris and a lens are used to concentrate light on the sample. The focused beam has a divergence angle of around 0.3° , smaller than the angular resolution of the rotation stage (1°). Both the PSG and PSA consist of a fixed linear polarizer and a rotating quarter-wave plate. Here, the two polarizers are aligned parallel to the horizontal direction, and the two wave plates are rotated in angular increments of five-to-one. The PSG prepares a set of polarization states, which then pass through the sample and get analyzed by the PSA.

Although Mueller polarimetry already provides complete information regarding the polarization properties of the sample, for illustration purposes, we also performed separate Stokes polarimetry to measure the output polarization for a fixed input polarization state. This is done using the same setup but without the quarter-wave plate in the PSG so that the incident polarization is fixed to be horizontal linear polarization.

SUPPLEMENTARY MATERIALS

Supplementary material for this article is available at <http://advances.sciencemag.org/cgi/content/full/6/23/eaba3367/DC1>

REFERENCES AND NOTES

- J. W. Anthony, R. A. Bideaux, K. W. Bladh, M. C. Nichols, *Handbook of Mineralogy* (Mineral Data Publishing, 1990), vol. 1.
- A. Ortigosa-Blanch, J. C. Knight, W. J. Wadsworth, J. Arriaga, B. J. Mangan, T. A. Birks, P. S. J. Russell, Highly birefringent photonic crystal fibers. *Opt. Lett.* **25**, 1325–1327 (2000).
- P.-L. Liu, B.-J. Li, Study of form birefringence in waveguide devices using the semivectorial beam propagation method. *IEEE Photonic. Tech. L.* **3**, 913–915 (1991).
- M. Khorasaninejad, W. T. Chen, R. C. Devlin, J. Oh, A. Y. Zhu, F. Capasso, Metalenses at visible wavelengths: Diffraction-limited focusing and subwavelength resolution imaging. *Science* **352**, 1190–1194 (2016).
- N. Yu, F. Capasso, Flat optics with designer metasurfaces. *Nat. Mater.* **13**, 139–150 (2014).
- D. Lin, P. Fan, E. Hasman, M. L. Brongersma, Dielectric gradient metasurface optical elements. *Science* **345**, 298–302 (2014).

- A. Arbabi, Y. Horie, M. Bagheri, A. Faraon, Dielectric metasurfaces for complete control of phase and polarization with subwavelength spatial resolution and high transmission. *Nat. Nanotechnol.* **10**, 937–943 (2015).
- J. P. Balthasar Mueller, N. A. Rubin, R. C. Devlin, B. Groever, F. Capasso, Metasurface polarization optics: Independent phase control of arbitrary orthogonal states of polarization. *Phys. Rev. Lett.* **118**, 113901 (2017).
- R. C. Devlin, A. Ambrosio, D. Wintz, S. L. Oscurato, A. Y. Zhu, M. Khorasaninejad, J. Oh, P. Maddalena, F. Capasso, Spin-to-orbital angular momentum conversion in dielectric metasurfaces. *Opt. Express* **25**, 377–393 (2017).
- Y.-W. Huang, N. A. Rubin, A. Ambrosio, Z. Shi, R. C. Devlin, C.-W. Qiu, F. Capasso, Versatile total angular momentum generation using cascaded J-plates. *Opt. Express* **27**, 7469–7484 (2019).
- N. A. Rubin, G. D'Aversa, P. Chevalier, Z. Shi, W. T. Chen, F. Capasso, Matrix Fourier optics enables a compact full-Stokes polarization camera. *Science* **365**, eaax1839 (2019).
- N. A. Rubin, A. Zaidi, M. Juhl, R. P. Li, J. P. B. Mueller, R. C. Devlin, K. Leósson, F. Capasso, Polarization state generation and measurement with a single metasurface. *Opt. Express* **26**, 21455–21478 (2018).
- R. A. Chipman, G. Young, W. S. T. Lam, *Polarized Light and Optical Systems, Optical Sciences and Applications of Light* (Taylor & Francis, CRC Press, 2018).
- J. N. Damask, *Polarization Optics in Telecommunications* (Springer Science & Business Media, 2004), vol. 101.
- A. Sit, L. Giner, E. Karimi, J. S. Lundeen, General lossless spatial polarization transformations. *J. Opt.* **19**, 094003 (2017).
- C. Guo, M. Xiao, M. Minkov, Y. Shi, S. Fan, Photonic crystal slab Laplace operator for image differentiation. *Optica* **5**, 251 (2018).
- M. Qiu, M. Jia, S. Ma, S. Sun, Q. He, L. Zhou, Angular dispersions in terahertz metasurfaces: Physics and applications. *Phys. Rev. Applied* **9**, 054050 (2018).
- S. M. Kamali, E. Arbabi, A. Arbabi, Y. Horie, M. S. Faraji-Dana, A. Faraon, Angle-multiplexed metasurfaces: Encoding independent wavefronts in a single metasurface under different illumination angles. *Phys. Rev. X* **7**, 041056 (2017).
- J. S. Jensen, O. Sigmund, Topology optimization for nano-photonics. *Laser Photonics Rev.* **5**, 308–321 (2011).
- C. M. Lalau-Keraly, S. Bhargava, O. D. Miller, E. Yablonovitch, Adjoint shape optimization applied to electromagnetic design. *Opt. Express* **21**, 21693–21701 (2013).
- S. Molesky, Z. Lin, A. Y. Piggott, W. Jin, J. Vucković, A. W. Rodriguez, Inverse design in nanophotonics. *Nat. Photonics* **12**, 659–670 (2018).
- S. D. Campbell, D. Sell, R. P. Jenkins, E. B. Whiting, J. A. Fan, D. H. Werner, Review of numerical optimization techniques for meta-device design [Invited]. *Opt. Mater. Express* **9**, 1842–1863 (2019).
- D. Sell, J. Yang, S. Doshay, R. Yang, J. A. Fan, Large-angle, multifunctional metagratings based on freeform multimode geometries. *Nano Lett.* **17**, 3752–3757 (2017).
- N. M. Estakhri, B. Edwards, N. Engheta, Inverse-designed metastructures that solve equations. *Science* **363**, 1333–1338 (2019).
- T. Phan, D. Sell, E. W. Wang, S. Doshay, K. Edee, J. Yang, J. A. Fan, High-efficiency, large-area, topology-optimized metasurfaces. *Light-Sci. Appl.* **8**, 48 (2019).
- C. Menzel, C. Rockstuhl, F. Lederer, Advanced Jones calculus for the classification of periodic metamaterials. *Phys. Rev. A* **82**, 053811 (2010).
- S. S. Kruk, A. N. Poddubny, D. A. Powell, C. Helgert, M. Decker, T. Pertsch, D. N. Neshev, Y. S. Kivshar, Polarization properties of optical metasurfaces of different symmetries. *Phys. Rev. B* **91**, 195401 (2015).
- A. Y. Zhu, W. T. Chen, A. Zaidi, Y.-W. Huang, M. Khorasaninejad, V. Sanjeev, C.-W. Qiu, F. Capasso, Giant intrinsic chiro-optical activity in planar dielectric nanostructures. *Light Sci. Appl.* **7**, 17158 (2018).
- S. S. Wang, R. Magnusson, Theory and applications of guided-mode resonance filters. *Appl. Optics* **32**, 2606–2613 (1993).
- D. H. Goldstein, Mueller matrix dual-rotating retarder polarimeter. *Appl. Optics* **31**, 6676–6683 (1992).
- P. Lalanne, J. P. Hugonin, P. Chavel, Optical properties of deep lamellar gratings: A coupled Bloch-mode insight. *J. Lightwave Technol.* **24**, 2442–2449 (2006).
- M. Bass, C. De Cusatis, J. Enoch, V. Lakshminarayanan, G. Li, C. M. Donald, V. Mahajan, E. Van Stryland, *Handbook of Optics, Third Edition Volume II: Design, Fabrication and Testing, Sources and Detectors, Radiometry and Photometry* (McGraw-Hill Inc., ed. 3, 2009).
- A. Argyros, J. Pla, F. Ladouceur, L. Poladian, Circular and elliptical birefringence in spun microstructured optical fibres. *Opt. Express* **17**, 15983–15990 (2009).
- N. Chateau, J.-P. Hugonin, Algorithm for the rigorous coupled-wave analysis of grating diffraction. *JOSA A* **11**, 1321–1331 (1994).

Acknowledgments: We acknowledge N. Rubin, V. Ginis, and X. Yin for helpful comments. Z.S. thanks Z. Dai for insightful discussions. **Funding:** This material is based on work supported by the Air Force Office of Scientific Research under award number FA9550-19-1-0135. C.-W.Q. and Y.W.H. acknowledge the support from the National Research Foundation, Prime Minister's

Office, Singapore, under its Competitive Research (CRP award no. NRF-CRP15-2015-03). A.Y.Z. thanks Harvard SEAS and A*STAR Singapore under the National Science Scholarship scheme. This work was performed in part at the Center for Nanoscale Systems (CNS), a member of the National Nanotechnology Coordinated Infrastructure (NNCI), which is supported by the National Science Foundation under NSF award no. 1541959. CNS is part of Harvard University.

Author contributions: Z.S. conceived the experiment and carried out analyses. A.Y.Z., Y.-W.H., and Z.S. fabricated the sample. Z.S. and Z.L. developed the optimization algorithm. Z.S. and W.T.C. performed experimental characterization. Z.S. prepared the original manuscript with significant contributions from A.Y.Z. and Y.-W.H. C.-W.Q. and F.C. supervised the project and participated in manuscript preparation. **Competing interests:** The authors declare that they have no competing interests. **Data and materials availability:** All data needed to evaluate

the conclusions in the paper are present in the paper and/or the Supplementary Materials. Additional data related to this paper may be requested from the authors.

Submitted 24 November 2019

Accepted 23 March 2020

Published 3 June 2020

10.1126/sciadv.aba3367

Citation: Z. Shi, A. Y. Zhu, Z. Li, Y.-W. Huang, W. T. Chen, C.-W. Qiu, F. Capasso, Continuous angle-tunable birefringence with freeform metasurfaces for arbitrary polarization conversion. *Sci. Adv.* **6**, eaba3367 (2020).

Continuous angle-tunable birefringence with freeform metasurfaces for arbitrary polarization conversion

Zhujun Shi, Alexander Y. Zhu, Zhaoyi Li, Yao-Wei Huang, Wei Ting Chen, Cheng-Wei Qiu and Federico Capasso

Sci Adv 6 (23), eaba3367.
DOI: 10.1126/sciadv.aba3367

ARTICLE TOOLS	http://advances.sciencemag.org/content/6/23/eaba3367
SUPPLEMENTARY MATERIALS	http://advances.sciencemag.org/content/suppl/2020/06/01/6.23.eaba3367.DC1
REFERENCES	This article cites 30 articles, 4 of which you can access for free http://advances.sciencemag.org/content/6/23/eaba3367#BIBL
PERMISSIONS	http://www.sciencemag.org/help/reprints-and-permissions

Use of this article is subject to the [Terms of Service](#)

Science Advances (ISSN 2375-2548) is published by the American Association for the Advancement of Science, 1200 New York Avenue NW, Washington, DC 20005. The title *Science Advances* is a registered trademark of AAAS.

Copyright © 2020 The Authors, some rights reserved; exclusive licensee American Association for the Advancement of Science. No claim to original U.S. Government Works. Distributed under a Creative Commons Attribution NonCommercial License 4.0 (CC BY-NC).